

Feasibility of Deep Learning-Guided Attenuation and Scatter Correction of Whole-Body ^{68}Ga -PSMA PET Studies in the Image Domain

Samaneh Mostafapour, MSc,* Faeze Gholamiankhah, MSc,† Habibollah Dadgar, MSc,‡
Hossein Arabi, PhD,§ and Habib Zaidi, PhD§||¶**

Objective: This study evaluates the feasibility of direct scatter and attenuation correction of whole-body ^{68}Ga -PSMA PET images in the image domain using deep learning.

Methods: Whole-body ^{68}Ga -PSMA PET images of 399 subjects were used to train a residual deep learning model, taking PET non-attenuation-corrected images (PET-nonAC) as input and CT-based attenuation-corrected PET images (PET-CTAC) as target (reference). Forty-six whole-body ^{68}Ga -PSMA PET images were used as an independent validation dataset. For validation, synthetic deep learning-based attenuation-corrected PET images were assessed considering the corresponding PET-CTAC images as reference. The evaluation metrics included the mean absolute error (MAE) of the SUV, peak signal-to-noise ratio, and structural similarity index (SSIM) in the whole body, as well as in different regions of the body, namely, head and neck, chest, and abdomen and pelvis.

Results: The deep learning-guided direct attenuation and scatter correction produced images of comparable visual quality to PET-CTAC images. It achieved an MAE, relative error (RE%), SSIM, and peak signal-to-noise ratio of 0.91 ± 0.29 (SUV), $-2.46\% \pm 10.10\%$, 0.973 ± 0.034 , and 48.171 ± 2.964 , respectively, within whole-body images of the independent external validation dataset. The largest RE% was observed in the head and neck region ($-5.62\% \pm 11.73\%$), although this region exhibited the highest value of SSIM metric (0.982 ± 0.024). The MAE (SUV) and RE% within the different regions of the body were less than 2.0% and 6%, respectively, indicating acceptable performance of the deep learning model.

Conclusions: This work demonstrated the feasibility of direct attenuation and scatter correction of whole-body ^{68}Ga -PSMA PET images in the image domain using deep learning with clinically tolerable errors. The technique has the potential of performing attenuation correction on stand-alone PET or PET/MRI systems.

Key Words: ^{68}Ga -PSMA, attenuation correction, deep learning, PET/CT, whole body

(*Clin Nucl Med* 2021;46: 609–615)

Prostate cancer is one of the most frequently diagnosed malignancies and the leading cause of death in men. It has been shown that the major cause of death in the United States in 2020 was lung, prostate, and colorectal cancer.¹ Prostate biopsy is commonly performed for definite confirmation of prostate cancer occurrence. However, this procedure is invasive. Noninvasive strategies are needed for early detection, accurate localization, staging, and treatment monitoring. Diagnostic procedures providing information regarding prostate-specific antigen, Gleason score, and lymph node invasion are often performed. Recent advances in medical imaging technologies, including PET, enabled noninvasive functional imaging of prostate cancer.^{2,3} Hybrid imaging using PET with dedicated molecular imaging probes combined with anatomical CT or MRI is regarded as an efficient modality for the diagnosis of the prostate cancer. In this regard, ^{68}Ga -labeled prostate-specific membrane antigen (PSMA) PET radiotracer has shown promising potential for timely diagnosis, staging, and therapy assessment of prostate cancer.^{4–6}

In PET, the interaction of annihilation photons with biological tissues causes significant signal loss, resulting in deterioration of image quality, poor contrast, and quantitative bias. Therefore, attenuation and scatter correction (AC) is crucial for reliable, reproducible, and accurate quantitative PET imaging.⁷ In hybrid PET/CT imaging, information about the attenuation properties of biological tissues and other objects and accessories present in the field of view, such as the scanner bed, is readily provided by CT images coded in Hounsfield units to create patient-specific PET attenuation maps. However, in hybrid PET/MRI, proton density and tissue relaxation times from MRI scans do not directly translate to photon attenuation coefficients. Hence, in the past decade, MRI-guided AC in PET/MRI systems has remained a challenging task, leading to various generic approaches to tackle this problem.^{8–11} These include segmentation-,¹² atlas-,¹³ emission-,¹⁴ and artificial intelligence-based^{15,16} AC approaches.

Segmentation-based methods classify the input MRI scans into major tissue classes to create a PET AC map through the assignment of predefined attenuation coefficients to each tissue class.^{17,18} Atlas-based methods rely on the prior knowledge extracted from coregistered MRI and CT atlas image pairs to predict a synthetic CT of the target MRI scan.^{19,20} However, these MRI-guided AC approaches are prone to remarkable errors due to the presence of anatomic abnormalities, intra-atlas misregistration, tissue misclassification, body truncation, image artifacts, noise, and inhomogeneity in MRI scans.^{16,21,22}

The incorporation of time-of-flight information into the maximum likelihood reconstruction of attenuation and activity map method (MLAA) enabled the prediction of patient-specific AC

Received for publication January 13, 2021; revision accepted January 22, 2021.

From the *Department of Radiology Technology, Faculty of Paramedical Sciences, Mashhad University of Medical Sciences, Mashhad; †Department of Medical Physics, Faculty of Medicine, Shahid Sadoughi University of Medical Sciences, Yazd; ‡Cancer Research Center, Razavi Hospital, Imam Reza International University, Mashhad, Iran; §Division of Nuclear Medicine and Molecular Imaging, Department of Medical Imaging, Geneva University Hospital, CH-1211 Geneva 4; ||Geneva University Neurocenter, Geneva University, Geneva, Switzerland; ¶Department of Nuclear Medicine and Molecular Imaging, University of Groningen, University Medical Center Groningen, Groningen, the Netherlands; and **Department of Nuclear Medicine, University of Southern Denmark, Odense, Denmark.

S.M. and F.G. contributed equally to this work.

Conflicts of interest and sources of funding: This work was supported by the Swiss National Science Foundation under grant SNRF 320030_176052, the Eurostars program of the European Commission under grant E!114021 ProVision, and the Private Foundation of Geneva University Hospitals under grant RC-06-01. None declared to all authors.

All procedures performed in studies involving human participants were under the ethical standards. Informed consent was obtained from all individual participants included in the study.

Correspondence to: Habib Zaidi, PhD, Division of Nuclear Medicine and Molecular Imaging, Department of Medical Imaging, Geneva University Hospital, CH-1211 Geneva, 4 Rue Gabrielle-Perret-Gentil, Switzerland. E-mail: habib.zaidi@hcuge.ch.

Copyright © 2021 Wolters Kluwer Health, Inc. All rights reserved.

ISSN: 0363-9762/21/4608-0609

DOI: 10.1097/RLU.0000000000003585

maps from the PET emission data. This method often suffers from high noise levels, activity-attenuation cross-talk, and quantitative uncertainty of the estimated attenuation coefficients.²³ To address these limitations, deep learning approaches were exploited to generate accurate synthetic CT images from the preliminary estimated AC maps using the MLAA method in whole-body ¹⁸F-FDG PET imaging.²⁴

The extraordinary processing power and the versatility of deep learning approaches have created a paradigm shift in the field of MRI-guided or transmissionless PET AC.^{25,26} These include novel frameworks to transform MRI to CT images in an end-to-end fashion,^{27–29} estimation of patient-specific attenuation correction factors from time-of-flight sinogram bins,³⁰ estimation of AC maps or synthetic CT images from non-AC PET images,³¹ and synthetic CT image prediction from preliminary MLAA-based estimation of PET AC maps.³² Moreover, direct attenuation and scatter correction in the image domain have been investigated in ¹⁸F-FDG PET brain imaging^{33,34} and whole-body imaging.^{35,36} This approach is of special interest because it does not require the availability of concurrent anatomical (CT or MRI) images. More importantly, it enables to correct for motion artifacts induced by mismatches between emission and transmission data.^{15,35} This approach was evaluated for multiple radiotracers in brain PET imaging.³⁷ Yet, in whole-body PET imaging, direct attenuation and scatter correction have only been assessed for ¹⁸F-FDG.

In this work, we set out to examine the accuracy of the direct attenuation and scatter correction in the image domain for the whole-body ⁶⁸Ga-PSMA PET imaging using a residual deep neural network. A deep learning model is trained to predict attenuation and scatter-corrected (PET-AC) ⁶⁸Ga-PSMA PET images directly from the corresponding non-attenuation-corrected ones in an end-to-end fashion. No anatomical images are used within the training of the model. CT-based attenuation and scatter-corrected (PET-CTAC) images are considered as standard of reference to evaluate the performance of the deep learning model.

PATIENTS AND METHODS

PET/CT Data Acquisition

A retrospective sample of 445 patients who underwent ⁶⁸Ga-PSMA PET/CT examinations between March 2015 and April 2020 was included in this study protocol. PET/CT examinations were performed on a Biograph 6 Truepoint (Siemens Healthcare) PET/CT scanner.

The patients were injected with 185 ± 21 MBq (2 MBq/kg) activity of ⁶⁸Ga-PSMA. Prior to PET acquisition, a low-dose CT scan was performed for attenuation correction 1 hour postinjection. CT images were acquired with the following parameters: tube potential of 110 kVp, tube current of 52 mAs, computed tomography dose index_volume of 3.96 mGy, dose length product of 453 mGy × cm, rotation time of 0.6 second, slice thickness of 4 mm, matrix size of 512 × 512, and a voxel size of $1.36 \times 1.36 \times 3$ mm³. CT-based PET attenuation and scatter-corrected (PET-CTAC) and non-attenuation-corrected PET images (PET-nonAC) were reconstructed using the ordinary Poisson ordered subsets expectation maximization algorithm with 2 iterations, 8 subsets, and a 5-mm postreconstruction Gaussian filter. The final reconstructed matrix size was 168 × 168 with a pixel size of $4.07 \times 4.07 \times 3$ mm³.

Network Architecture

To predict PET-CTAC from PET-nonAC images in an end-to-end fashion without employing anatomical images, a ResNet model implemented in the NiftyNet platform was utilized. NiftyNet is an open-source pipeline built upon TensorFlow for the realization of deep learning models. The NiftyNet infrastructure consists of state-of-the-art convolutional neural network architectures that can be rapidly retrieved and optimized for different medical image analysis applications, including segmentation, regression, and image synthesis.³⁸

The ResNet architecture³⁹ depicted in Figure 1 consists of 20 convolutional layers wherein each layer is composed of an element-wise rectified linear unit (ReLU) and a batch normalization layer. Every 2 convolutional layers are linked together by residual connections to build residual blocks. In the first seven 3 × 3 × 3-voxel convolution kernel layers, a 3 × 3 × 3-voxel kernel is used to encode low-level features, such as edges and corners from the input image. For extracting midlevel and high-level features, the kernel is dilated by factors of 2 and 4 in the following 7 and 6 layers, respectively. Because this residual network retains the spatial resolution of the input images throughout the network, the output of the final layer, which is a fully connected softmax layer, has a dimension equal to that of the input image.³⁹

Implementation Details

Prior to the training of the model, the voxel values of all PET images were converted to SUV to reduce the dynamic range of image intensities. Furthermore, the intensities of PET images were scaled down using empirical factors of 8 and 3 for PET-CTAC

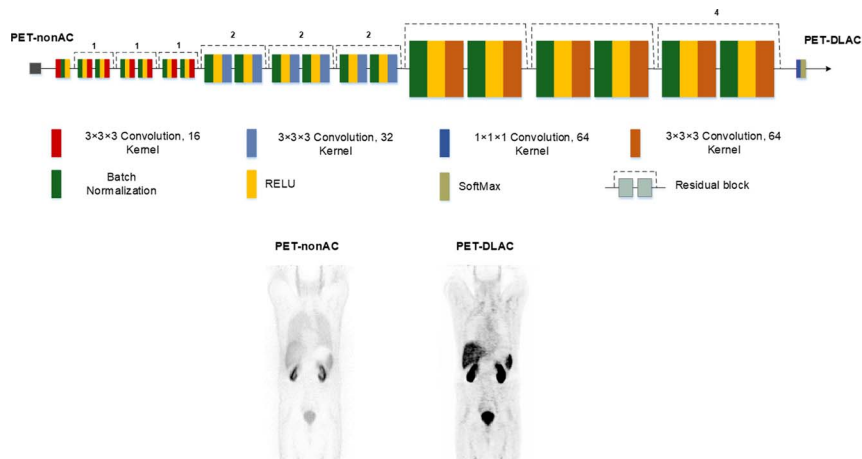


FIGURE 1. Architecture of ResNet network implemented in the NiftyNet platform used in this work.³⁹

and PET-nonAC images, respectively. Subsequently, all images were cropped into a matrix size of 72×136 voxels to eliminate irrelevant background air and reduce the computational burden.

To train the ResNet model, pairs of PET-nonAC and PET-CTAC images were considered as input and output of the ResNet model, respectively. Of the 445 ^{68}Ga -PSMA whole-body PET studies included in this study, 399 subjects were randomly selected for training and 46 subjects for validation (external validation dataset) of the model. The training was performed using a 2-dimensional spatial window equal to 72×136 voxels wherein each pair of PET-CTAC and PET-nonAC 2D transaxial slices was considered as a single training sample. The following parameters were set for the training of the ResNet model: learning rate = 0.001, optimizer = Adam, loss function = L2 loss, decay = 0.0001, batch size = 45, sample per volume = 1, and queue length = 300. To check potential overfitting, 5% of the training dataset was dedicated to the evaluation of the model within the training. Insignificant differences were observed between the evaluation and training losses (errors), which indicates no risk of overfitting. The training of the ResNet was almost completed in 4 epochs as the training loss reached its plateau.

Evaluation Strategy

To evaluate the performance of attenuation and scatter correction in the image domain, deep learning-based attenuation-corrected PET images (PET-DLAC) were compared with reference PET-CTAC images for the 46 patients consisting the external test dataset. All PET images were segmented into 3 regions including head and neck, chest, and abdomen and pelvis for region-based analysis. The quality and the quantitative accuracy of the synthesized ^{68}Ga -PSMA whole-body PET images were assessed over the whole-body area, as well as the different segmented regions using voxel-wise mean error (ME) (Eq. 1), mean absolute error (MAE) (Eq. 2), mean square error (MSE) (Eq. 3), root mean square error (RMSE) (Eq. 4), and relative error (RE%) (Eq. 5) calculated between PET-CTAC and PET-DLAC images:

$$\text{ME} = \frac{1}{V} \sum_{i=1}^V (\text{PET}_{\text{DLAC}}(i) - \text{PET}_{\text{CTAC}}(i)) \quad (1)$$

$$\text{MAE} = \frac{1}{V} \sum_{i=1}^V |\text{PET}_{\text{DLAC}}(i) - \text{PET}_{\text{CTAC}}(i)| \quad (2)$$

$$\text{MSE} = \frac{1}{V} \sum_{i=1}^V (\text{PET}_{\text{DLAC}}(i) - \text{PET}_{\text{CTAC}}(i))^2 \quad (3)$$

$$\text{RMSE} = \sqrt{\frac{1}{V} \sum_{i=1}^V (\text{PET}_{\text{DLAC}}(i) - \text{PET}_{\text{CTAC}}(i))^2} \quad (4)$$

$$\text{RE}(\%) = \frac{1}{V} \sum_{i=1}^V \frac{\text{PET}_{\text{DLAC}}(i) - \text{PET}_{\text{CTAC}}(i)}{\text{PET}_{\text{CTAC}}} \times 100 \quad (5)$$

Here, V indicates the total number of voxels in the volume of interest, whereas i stands for the corresponding i th voxel in PET-DLAC and PET-CTAC images.

Furthermore, the peak signal-to-noise ratio (PSNR) and structural similarity index (SSIM) were calculated between the predicted PET-DLAC and PET-CTAC images using Eqs. 6 and 7, respectively.

$$\text{PSNR} = 10 \log \left(\frac{I^2}{\text{MSE}} \right) \quad (6)$$

$$\text{SSIM} = \frac{(2\mu_{\text{CTAC}}\mu_{\text{DLAC}} + K_1)(2\delta_{\text{CTAC,DLAC}} + K_2)}{(\mu_{\text{CTAC}}^2 + \mu_{\text{DLAC}}^2 + K_1)(\delta_{\text{CTAC}}^2 + \delta_{\text{DLAC}}^2 + K_2)} \quad (7)$$

In Eq. 6, I represents the maximum intensity value of PET-CTAC or PET-DLAC, whereas MSE stands for the MSE. In Eq. 7, μ_{CTAC} and μ_{DLAC} denote the mean value of PET-CTAC and PET-DLAC images, respectively. δ_{CTAC} and δ_{DLAC} are the variances of PET-CTAC and PET-DLAC images, whereas $\delta_{\text{CTAC,DLAC}}$ indicates their covariance. The parameters $K_1 = (k_1 I)^2$ and $K_2 = (k_2 I)^2$ with constants $k_1 = 0.01$ and $k_2 = 0.02$ were introduced to avoid division by very small values.

Moreover, the voxel-wise distribution of tracer uptake correlation between PET-DLAC and reference PET-CTAC images was evaluated using joint histogram analysis (with Pearson correlation) within an SUV range of 0.1 to 18 in 200 bins.

RESULTS

Representative coronal views of PET-nonAC, PET-CTAC, and PET-DLAC images, along with the corresponding CT image, are illustrated in Figure 2. Moreover, the bias map calculated between PET-DLAC and reference PET-CTAC images (exhibiting the absolute overestimation/underestimation of the activity concentration) is shown in Figure 2E. Visual inspection revealed good agreement in terms of image quality, texture, and structural similarity between PET-DLAC and PET-CTAC images.

Table 1 summarizes the mean and SD of the quantitative metrics, including ME, MAE, MSE, RMSE, RE, PSNR, and SSIM,

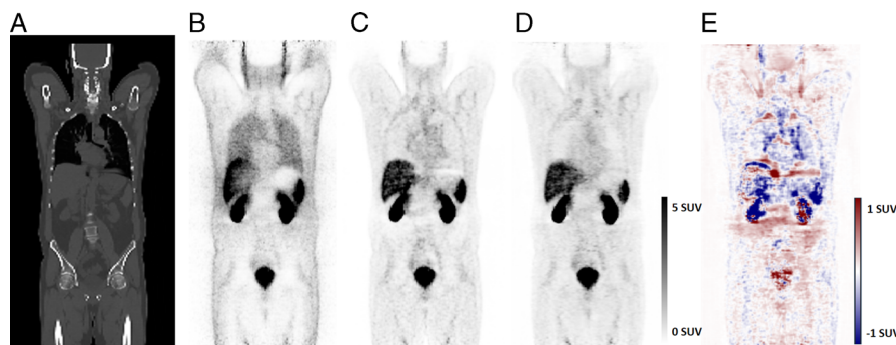


FIGURE 2. Representative coronal views of (A) CT, (B) PET-nonAC, (C) PET-CTAC, (D) PET-DLAC images, and (E) the difference bias map calculated as PET-DLAC – PET-CTAC.

TABLE 1. Statistical Analysis of Image Quality Metrics (ME, MAE, MSE, RE, PSNR, SSIM) Calculated Within the Different Regions of the Body in PET-DLAC Images With Respect to Reference PET-CTAC Images

Regions	ME (SUV)	MAE (SUV)	MSE	RMSE (SUV)	RE%	PSNR	SSIM
Head and neck	0.06 ± 0.21	0.67 ± 0.15	0.032 ± 0.019	0.172 ± 0.047	-5.63 ± 11.73	44.4 ± 2.56	0.982 ± 0.024
Chest	-0.15 ± 0.30	0.75 ± 0.24	0.031 ± 0.042	0.160 ± 0.072	-1.89 ± 10.91	30.55 ± 5.77	0.947 ± 0.067
Abdomen and pelvis	-0.36 ± 0.56	1.17 ± 0.40	0.177 ± 0.168	0.393 ± 0.148	-2.18 ± 12.36	45.91 ± 2.79	0.969 ± 0.040
Whole body	-0.11 ± 0.42	0.91 ± 0.29	0.108 ± 0.109	0.304 ± 0.123	-2.47 ± 10.10	48.17 ± 2.96	0.973 ± 0.034

calculated between SUV images of PET-CTAC and PET-DLAC images across the 46 patients of the external validation dataset. The quantitative metrics are reported separately for the whole-body and the different regions of the body. Overall, the chest, head and neck, whole-body, and abdomen and pelvis regions ranked from the highest to lowest in terms of ME, MAE, and RMSE metrics. The DLAC method led to relatively small errors within the head and neck and chest regions. However, larger errors were observed within the abdomen and pelvis region. The ME, MAE, and RMSE values in the abdomen and pelvis region were -0.36 ± 0.056 (SUV), 1.17 ± 0.040 (SUV), and 0.177 ± 0.168 (SUV), respectively. The RE% revealed underestimation of SUV in the head and neck ($-5.63\% \pm 11.73\%$), chest ($-1.89\% \pm 10.91\%$), abdomen and pelvis ($-2.18\% \pm 12.36\%$), and whole-body ($-2.47\% \pm 10.10\%$)

regions. The smallest REs were observed within the chest region. The DLAC resulted in PSNR of 44.36 ± 2.56 , 30.55 ± 5.77 , 45.91 ± 2.79 , and 48.17 ± 2.96 , and SSIM of 0.982 ± 0.024 , 0.947 ± 0.067 , 0.969 ± 0.040 , and 0.973 ± 0.034 in the head and neck, chest, abdomen and pelvis, and whole-body regions, respectively.

Figure 3 depicts coronal views of CT, PET-nonAC, PET-CTAC, and PET-DLAC images, along with a horizontal profile drawn through a malignant lesion located in the right lung on PET-nonAC, PET-CTAC, and PET-DLAC images. The profile of PET-DLAC agrees well with that of PET-CTAC in both high and low activity concentration areas of the right lung.

Figure 4 shows separately box plots of ME, MAE, SSIM, MSE, RMSE, PSNR, and RE metrics calculated within the different

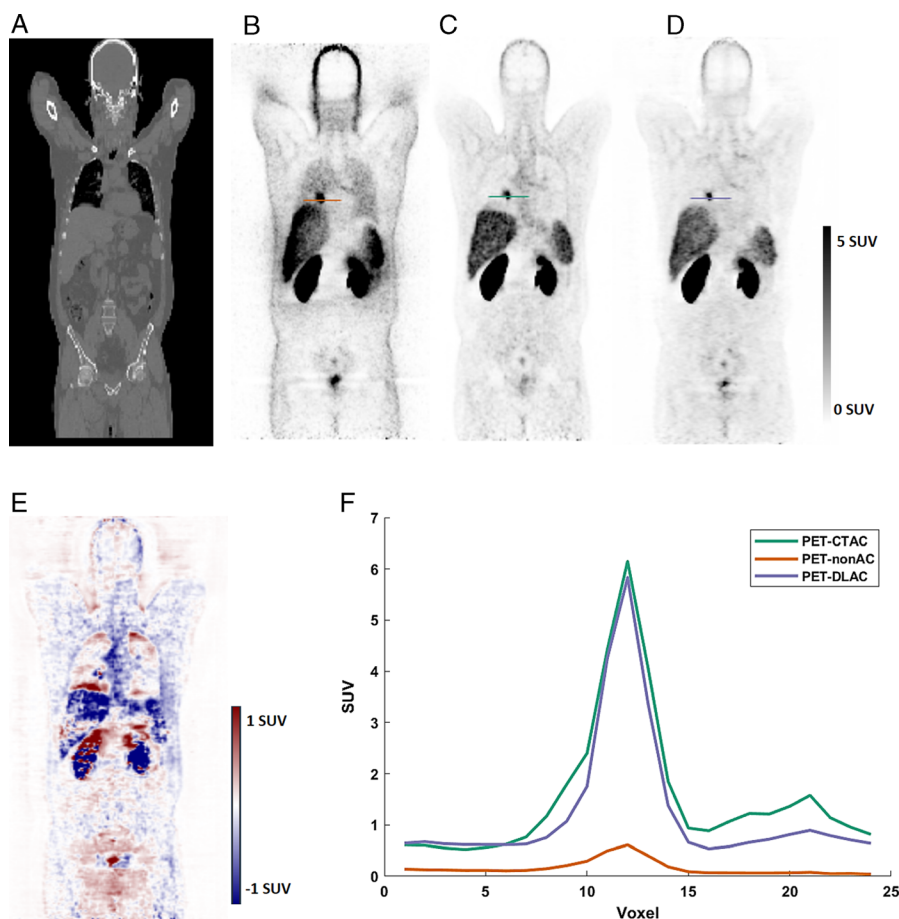


FIGURE 3. Coronal views of (A) CT, (B) PET-nonAC, (C) PET-CTAC, (D) PET-DLAC, and (E) the difference bias map calculated as PET-DLAC - PET-CTAC for a clinical study presenting with a malignant lesion in the right lung. (F) Horizontal profiles drawn through the lung lesion on the 3 PET images.

body regions. The highest MAE was observed in the abdomen and pelvis region, having the largest SD and outliers compared with other regions.

Furthermore, a voxel-wise assessment of the activity concentration was performed through joint histogram analysis of PET-DLAC versus reference PET-CTAC images. Figure 5 illustrates the high SUV correlation and voxel-wise similarity between the 2 attenuation correction methods with a correlation coefficient of $R^2 = 0.99$ and slope of 0.99.

DISCUSSION

The aim of this study was to assess the feasibility of direct attenuation and scatter correction of whole-body ^{68}Ga -PSMA PET studies in the image domain without using anatomical information. The deep learning-based attenuation and scatter correction model was evaluated on 46 subjects constituting the external validation dataset. Taking PET-CTAC images as reference, well-established quantitative metrics, including ME, MAE, and RE%, were computed to evaluate the performance of the proposed deep learning

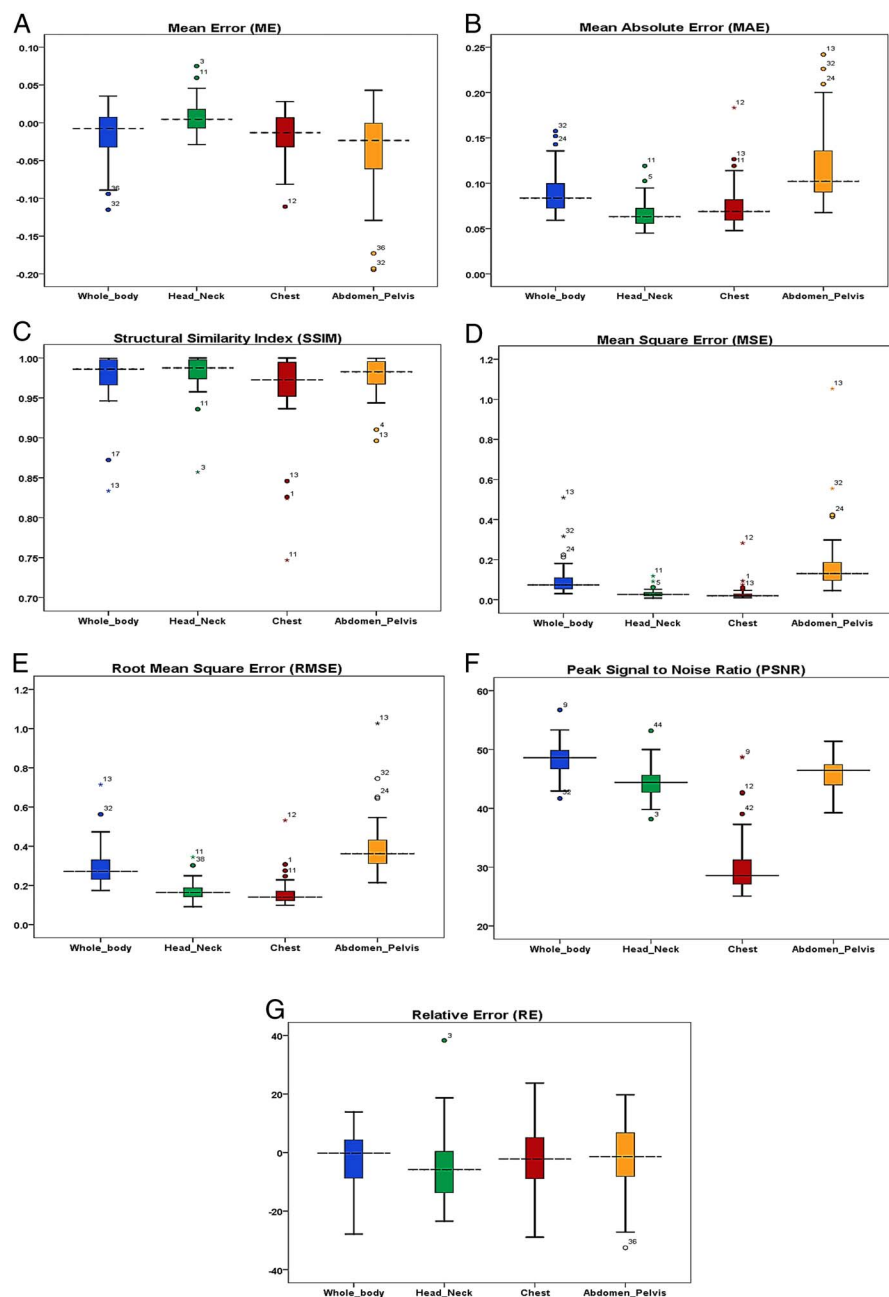


FIGURE 4. Comparison of (A) ME, (B) MAE, (C) SSIM, (D) MSE, (E) RMSE, (F) peak signal to noise ratio (PSNR), and (G) RE% calculated in PET-DLAC images (against reference PET-CTAC) within the different body regions. The box plots display the interquartile range (IQR), minimum ($Q1 - 1.5 \times IQR$), first quartile (Q1), median, third quartile (Q3), maximum ($Q3 + 1.5 \times IQR$), and outliers.

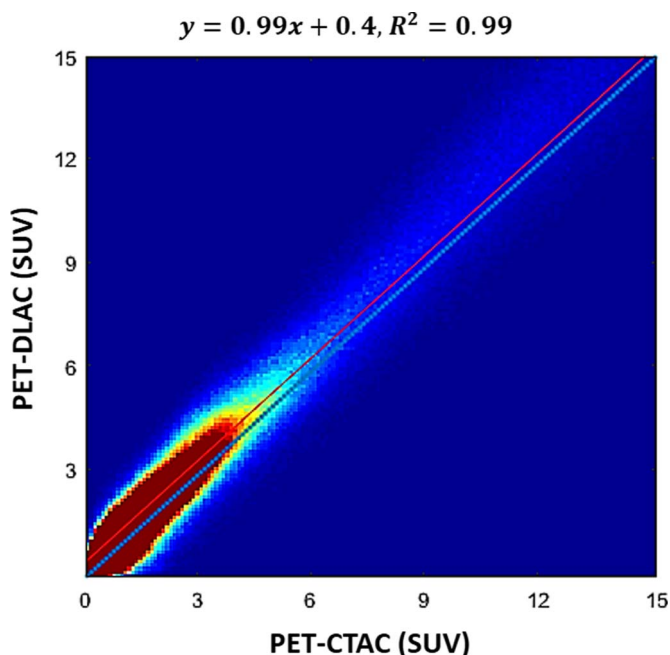


FIGURE 5. Joint histogram analysis of the voxel-wise SUV correlation between PET-DLAC and reference PET-CTAC images.

model. This study used a relatively large cohort of patients with normal/realistic anatomical and pathological variations for the training and evaluation of the deep learning model to guarantee a clinically relevant assessment of this AC framework.

MRI-guided attenuation correction methods face a number of challenges, including the lack of direct relationship between MRI intensities and linear attenuation coefficients of biological tissues, internal organs motion due to involuntary movement such as respiration, body truncation artifacts owing to the limited transaxial field of view of MRI, metal-induced artifacts,¹⁶ and increased acquisition time due to the use of dedicated MRI pulse sequences (such as ultrashort echo-time and zero echo-time) for bone segmentation.^{29,40} Regarding the fact that AC in the image domain relies solely on PET emission data, the mismatches between MRI- or CT-derived AC maps and PET emission data (due to body truncation or respiratory motion) would not affect the accuracy of PET AC.^{15,30,35} Deep learning techniques exhibited promising potential for the generation of AC maps from MRI scans compared with other approaches, including segmentation-based, atlas-based, and joint emission and transmission reconstruction approaches.^{8,24} Nevertheless, MRI-guided AC approaches (deep learning-, segmentation-, or atlas-based methods) are generally vulnerable to mismatches between PET emission data and anatomical information, which might result in gross PET quantification bias.^{16,41}

A previously proposed MRI-based AC method, combining atlas and pattern-recognition techniques, led to a mean RE% of $7.7\% \pm 8.4\%$ calculated over the whole body in ¹⁸F-FDG PET imaging, with the maximum errors being observed in the lung region.⁴² Hwang et al²⁴ used the activity and attenuation maps estimated through the MLAA algorithm to train a deep learning model to generate patient-specific AC maps (or synthetic CTs). This approach is also in principle immune to mismatches between PET emission and anatomical data. Yet, the algorithm is computationally demanding.

Dong et al¹⁵ extracted 3-dimensional patches from PET-nonAC and PET-CTAC images to train a CycleGAN architecture to model the impact of the attenuation and scatter in ¹⁸F-FDG PET imaging. They

achieved an RE of $0.62\% \pm 1.26\%$ over the whole body for ¹⁸F-FDG. In ¹⁸F-FDG brain imaging, a deep learning-based model was proposed by Yang et al³³ for an end-to-end conversion of PET-nonAC to PET-CTAC images using 35 clinical studies. They achieved an average SUV difference of 0.20 ± 0.92 calculated over 116 anatomical brain regions. Likewise, Shiri et al³⁵ employed a ResNet model to estimate PET attenuation-corrected from non-AC images in whole-body ¹⁸F-FDG imaging. The model training was performed in 2- and 3-dimensional modes wherein the 2-dimensional model (slice-by-slice training) exhibited superior performance with the highest mean RE% of $15.16\% \pm 3.96\%$ observed in the abdomen region. They trained the model using 1,000 whole-body PET scans and concluded that AC in the image domain is capable of accounting for patient's bulk and respiratory motions.

To the best of our knowledge, this is the first study dealing with attenuation correction of ⁶⁸Ga-PSMA whole-body PET scans in the image domain. Hence, the results obtained in this work are not directly comparable to those of other similar studies. Nevertheless, the magnitude of errors and the absolute SUV differences observed in this study indicate that this approach would enable the synthesis of whole-body ⁶⁸Ga-PSMA PET images with clinically tolerable errors.

The largest errors were observed in the abdomen and pelvis region, which is mostly due to the extremely large activity concentration in the bladder and suboptimal scatter correction in some clinical studies. The halo artifacts caused by imperfect scatter correction⁴³ were observed in some reference PET-CTAC images, which led to noticeably large errors in the synthesized PET-DLAC images. It should be noted that because only a small portion of the training dataset was corrupted with the halo artifact, the DLAC model was virtually insensitive to this artifact. As such, the manifestation of the halo artifact in the resulting PET-DLAC images was much less prominent compared with PET-CTAC images.

A major limitation of this work is the lack of clinical assessment of the proposed AC method. A systematic clinical evaluation of the synthesized PET images, for instance, in terms of visual image quality, lesion detectability, conspicuity, and clinical diagnosis or disease grading is warranted for a comprehensive evaluation of this approach. Moreover, a study of the impact of image artifacts and comparison to other MRI-guided and/or deep learning-based methods would give useful insight into the overall performance of this approach.

CONCLUSIONS

The present study demonstrated the feasibility of attenuation and scatter correction of whole-body ⁶⁸Ga-PSMA PET studies in the image domain without the use of anatomical imaging. The deep learning-based AC model exhibited excellent agreement between PET-DLAC and reference PET-CTAC images with a maximum mean SUV difference of 1.17 ± 0.40 and RE% of less than 6%. In this regard, the proposed deep learning model could be used in PET/MRI and stand-alone PET-only whole-body ⁶⁸Ga-PSMA PET imaging.

REFERENCES

1. Siegel RL, Miller KD, Goding Sauer A, et al. Colorectal cancer statistics, 2020. *CA Cancer J Clin.* 2020;70:145–164.
2. Kwan TN, Spremo S, Teh AY, et al. Performance of Ga-68 PSMA PET/CT for diagnosis and grading of local prostate cancer [published online August 10, 2020]. *Prostate Int.* 2021; In press.
3. Rayn KN, Elnabawi YA, Sheth N. Clinical implications of PET/CT in prostate cancer management. *Transl Androl Urol.* 2018;7:844–854.
4. van Leeuwen PJ, Stricker P, Hruby G, et al. (68)Ga-PSMA has a high detection rate of prostate cancer recurrence outside the prostatic fossa in patients being considered for salvage radiation treatment. *BJU Int.* 2016;5:732–739.

5. Maurer T, Gschwend JE, Rauscher I, et al. Diagnostic efficacy of (68)gallium-PSMA positron emission tomography compared to conventional imaging for lymph node staging of 130 consecutive patients with intermediate to high risk prostate cancer. *J Urol*. 2015;195:1436–1443.
6. Virgolini I, Decristoforo C, Haug A, et al. Current status of theranostics in prostate cancer. *Eur J Nucl Med Mol Imaging*. 2018;45:471–495.
7. Domachevsky L, Goldberg N, Gorenberg M, et al. Prostate cancer evaluation using PET quantification in ⁶⁸Ga-PSMA-11 PET/MR with attenuation correction of bones as a fifth compartment. *Quant Imaging Med Surg*. 2020;10:40–47.
8. Arabi H, Dowling JA, Burgos N, et al. Comparative study of algorithms for synthetic CT generation from MRI: consequences for MRI-guided radiation planning in the pelvic region. *Med Phys*. 2018;45:5218–5233.
9. Bogdanovic B, Gafita A, Schachoff S, et al. Almost 10 years of PET/MR attenuation correction: the effect on lesion quantification with PSMA: clinical evaluation on 200 prostate cancer patients. *Eur J Nucl Med Mol Imaging*. 2021;48:543–553.
10. Chen Y, An H. Attenuation correction of PET/MR imaging. *Magn Reson Imaging Clin N Am*. 2017;25:245–255.
11. Mehranian A, Arabi H, Zaidi H. Vision 20/20: magnetic resonance imaging-guided attenuation correction in PET/MRI: challenges, solutions, and opportunities. *Med Phys*. 2016;43:1130–1155.
12. Arabi H, Rager O, Alem A, et al. Clinical assessment of MR-guided 3-class and 4-class attenuation correction in PET/MR. *Mol Imaging Biol*. 2015;17:264–276.
13. Arabi H, Zaidi H. Comparison of atlas-based techniques for whole-body bone segmentation. *Med Image Anal*. 2017;36:98–112.
14. Mehranian A, Zaidi H. Joint estimation of activity and attenuation in whole-body TOF PET/MRI using constrained Gaussian mixture models. *IEEE Trans Med Imaging*. 2015;34:1808–1821.
15. Dong X, Lei Y, Wang T, et al. Deep learning-based attenuation correction in the absence of structural information for whole-body positron emission tomography imaging. *Phys Med Biol*. 2020;65:055011.
16. Arabi H, Zaidi H. Truncation compensation and metallic dental implant artefact reduction in PET/MRI attenuation correction using deep learning-based object completion. *Phys Med Biol*. 2020;65:195002.
17. Arabi H, Zaidi H. Whole-body bone segmentation from MRI for PET/MRI attenuation correction using shape-based averaging. *Med Phys*. 2016;43:5848–5861.
18. Ladefoged CN, Benoit D, Law I, et al. Region specific optimization of continuous linear attenuation coefficients based on UTE (RESOLUTE): application to PET/MR brain imaging. *Phys Med Biol*. 2015;60:8047–8065.
19. Arabi H, Zaidi H. Magnetic resonance imaging-guided attenuation correction in whole-body PET/MRI using a sorted atlas approach. *Med Image Anal*. 2016;31:1–15.
20. Arabi H, Zaidi H. One registration multi-atlas-based pseudo-CT generation for attenuation correction in PET/MRI. *Eur J Nucl Med Mol Imaging*. 2016;43:2021–2035.
21. Arabi H, Koutsouvelis N, Rouzaud M, et al. Atlas-guided generation of pseudo-CT images for MRI-only and hybrid PET-MRI-guided radiotherapy treatment planning. *Phys Med Biol*. 2016;61:6531–6552.
22. Zhuang M, Karakatsanis NA, Dierckx RAJO, et al. Impact of tissue classification in MRI-guided attenuation correction on whole-body Patlak PET/MRI. *Mol Imaging Biol*. 2019;21:1147–1156.
23. Mehranian A, Arabi H, Zaidi H. Quantitative analysis of MRI-guided attenuation correction techniques in time-of-flight brain PET/MRI. *Neuroimage*. 2016;130:123–133.
24. Hwang D, Kang SK, Kim KY, et al. Generation of PET attenuation map for whole-body time-of-flight ¹⁸F-FDG PET/MRI using a deep neural network trained with simultaneously reconstructed activity and attenuation maps. *J Nucl Med*. 2019;60:1183–1189.
25. Arabi H, Zaidi H. Applications of artificial intelligence and deep learning in molecular imaging and radiotherapy. *Eur J Hybr Imaging*. 2020;4:17.
26. Lee JS. A review of deep learning-based approaches for attenuation correction in positron emission tomography. *IEEE Trans Rad Plasma Med Sci*. 2021;4. doi:10.1109/TRPMS.2020.3009269.
27. Arabi H, Zeng G, Zheng G, et al. Novel adversarial semantic structure deep learning for MRI-guided attenuation correction in brain PET/MRI. *Eur J Nucl Med Mol Imaging*. 2019;46:2746–2759.
28. Bahrami A, Karimian A, Fatemizadeh E, et al. A new deep convolutional neural network design with efficient learning capability: application to CT image synthesis from MRI. *Med Phys*. 2020;47:5158–5171.
29. Ladefoged CN, Hansen AE, Henriksen OM, et al. AI-driven attenuation correction for brain PET/MRI: clinical evaluation of a dementia cohort and importance of the training group size. *Neuroimage*. 2020;222:117221.
30. Arabi H, Zaidi H. Deep learning-guided estimation of attenuation correction factors from time-of-flight PET emission data. *Med Image Anal*. 2020;64:101718.
31. Dong X, Wang T, Lei Y, et al. Synthetic CT generation from non-attenuation corrected PET images for whole-body PET imaging. *Phys Med Biol*. 2019;64:215016.
32. Shi L, Onofrey JA, Revilla EM, et al. A novel loss function incorporating imaging acquisition physics for PET attenuation map generation using deep learning. In: *International Conference on Medical Image Computing and Computer-Assisted Intervention*. Springer, Cham (MICCAI 2019): Springer; 2019:723–731.
33. Yang J, Park D, Gullberg GT, et al. Joint correction of attenuation and scatter in image space using deep convolutional neural networks for dedicated brain ¹⁸F-FDG PET. *Phys Med Biol*. 2019;64:075019.
34. Shiri I, Ghafarian P, Geramifar P, et al. Direct attenuation correction of brain PET images using only emission data via a deep convolutional encoder-decoder (deep-DAC). *Eur Radiol*. 2019;29:6867–6879.
35. Shiri I, Arabi H, Geramifar P, et al. Deep-JASC: joint attenuation and scatter correction in whole-body ¹⁸F-FDG PET using a deep residual network. *Eur J Nucl Med Mol Imaging*. 2020;47:2533–2548.
36. Dong X, Lei Y, Wang T, et al. Deep learning-based attenuation correction in the absence of structural information for whole-body positron emission tomography imaging. *Phys Med Biol*. 2020;65:055011.
37. Arabi H, Bortolin K, Ginovart N, et al. Deep learning-guided joint attenuation and scatter correction in multitracers neuroimaging studies. *Hum Brain Mapp*. 2020;41:3667–3679.
38. Gibson E, Li W, Sudre C, et al. NiftyNet: a deep-learning platform for medical imaging. *Comput Methods Programs Biomed*. 2018;158:113–122.
39. Li W, Wang G, Fidon L, et al. On the compactness, efficiency, and representation of 3D convolutional networks: brain parcellation as a pretext task. In: *International Conference on Information Processing in Medical Imaging*. Springer; 2017:348–360.
40. Pozaruk A, Pawar K, Li S, et al. Augmented deep learning model for improved quantitative accuracy of MR-based PET attenuation correction in PSMA PET-MRI prostate imaging. *Eur J Nucl Med Mol Imaging*. 2021;48:9–20.
41. Lu Y, Fontaine K, Mulnix T, et al. Respiratory motion compensation for PET/CT with motion information derived from matched attenuation-corrected gated PET data. *J Nucl Med*. 2018;59:1480–1486.
42. Hofmann M, Bezrukov I, Mantlik F, et al. MRI-based attenuation correction for whole-body PET/MRI: quantitative evaluation of segmentation- and atlas-based methods. *J Nucl Med*. 2011;52:1392–1399.
43. Heußer T, Mann P, Rank CM, et al. Investigation of the halo-artifact in ⁶⁸Ga-PSMA-11-PET/MRI. *PLoS One*. 2017;12:e0183329.